Controlling dendrite propagation in solid-state batteries with engineered stress

Cole D. Fincher[1], Christos E. Athanasiou[2,3], Colin Gilgenbach[1], Michael Wang[1], Brian W. Sheldon[2], W. Craig Carter[1], Yet-Ming Chiang[1]*

[1]Department of Materials Science and Engineering, Massachusetts Institute of Technology, Cambridge, MA, USA
[2]School of Engineering, Brown University, Providence, RI, USA
[3]Center for Bits and Atoms, Massachusetts Institute of Technology, Cambridge, MA, USA
*Email: ychiang@mit.edu

Abstract

Metal dendrite penetration is a mode of electrolyte failure that threatens the viability of metal anode based high energy solid-state batteries. Whether dendrites are driven by mechanical failure or electrochemical degradation of solid electrolytes remains an open question. If internal mechanical forces drive failure, superimposing an external compressive load that counters internal stress may mitigate dendrite penetration. Here, we investigate this hypothesis by dynamically applying mechanical loads to growing lithium metal dendrites in $Li_{6.75}La_3Zr_{1.75}Ta_{0.25}O_{12}$ solid electrolytes. *Operando* microscopy reveals marked deflection in the dendrite growth trajectory at the onset of compressive loading. At loads near 200 MPa, this deflection is sufficient to avert cell failure. Using fracture mechanics, we quantify the impact of stack pressure and in-plane stresses on dendrite trajectory, chart the residual stresses required to prevent short-circuit failure, and propose cell design approaches to achieve such stresses. The model and experiments show that in the materials studied here, dendrite propagation is dictated by fracture of the electrolyte and that electronic conductivity plays a negligible role.

Main

Pairing Li metal with non-flammable solid-electrolytes promises to enable safer and higher energy density batteries than Li-ion cells using flammable liquid electrolytes.[1] However, at practical current densities, metal filaments (generally referred to as dendrites) are known to pierce solid electrolytes and short-circuit cells.[1,2] Despite extensive study beginning nearly 50 years ago,[3–9] there is disagreement as to the mechanism(s) by which dendrites penetrate inorganic electrolytes. Most recent studies argue that failure occurs via one of two mechanisms. The first interpretation, based on the low fracture toughness of inorganic solid electrolytes and the crack-like morphology of many metal dendrites,[8,10–12] holds that metal dendrite penetration is driven by mechanical fracture: that metal insertion into flaws in the electrolyte at the metal – solid electrolyte interface leads to stress buildup exceeding the fracture strength of the solid electrolyte.[4,8,9,11,13] A second conjecture, based upon observations of Li metal nucleation within the bulk of the electrolyte, posits that failure is driven by electrical and electrochemical degradation: that electronic conduction enables internal reduction of lithium ions causing solid-phase Li metal to form within the solid electrolyte.[3,5,6] To design future electrolytes which are resistant to dendrites, the fundamental drivers underlying dendrite growth must be understood.

We develop an experimental methodology and fracture-mechanics model that elucidates the interaction between the electrochemical and mechanical forces underlying metal-dendrite propagation. We observe the propagation of lithium metal dendrites through a model solid electrolyte, $Li_{6.75}La_3Zr_{1.75}Ta_{0.25}O_{12}$ (LLZTO), under sequential and simultaneous electrochemical and mechanical stimulation. Using fracture mechanics, we predict the mechanical stress state required to arrest or deflect dendrites, and compare those results to experiments. Finally, we propose a design strategy that would

deflect or arrest dendrites by introducing residual compressive stresses into the electrolyte during the fabrication of solid-state batteries.

Response of metal dendrites to electrical and mechanical stimulation

If plating-induced pressure (P in Fig. 1b) drives dendrite growth, superimposing a compressive stress ($\sigma_{applied}$ in Fig. 1c) should balance internal stress buildup and mitigate penetration. We investigate this hypothesis by applying stresses mechanically, but such stresses could also be produced with residual thermal or chemically-induced stresses. Using a geometry in which two lithium metal electrodes are adhered to the surface of a thin disc of LLZTO electrolyte, we plate lithium through the plane of the electrolyte. Using a geometry in which two lithium metal electrodes are adhered to the surface of a thin disc of LLZTO electrolyte, we plate lithium dendrites through the plane of the electrolyte. This solid-state cell (~1.27 cm diameter) is mounted on a cantilever beam (Fig. 1a and Fig. 1b), oriented such that bending the beam results in an applied stress $\sigma_{applied}$ orthogonal to the electric field direction (Fig. 1c). By using a transparent material for the cantilever beam, *operando* optical microscopy can be conducted while varying current and mechanical load independently.

We observed that metal dendrites exhibit a correlated response to applied mechanical loads (Figs. 2 – 4). Results for a 90 µm thick LLZTO electrolyte disc are shown in Figure 2. A dendrite propagating under 0.2 mA/cm^2 current density (current divided by the initial Li metal electrode area) was subjected to 70 MPa applied compression, and then unloaded. The path of the dendrite under no applied load is highlighted in blue, while the segment propagated under load is highlighted in red. Micrographs with no highlighting are shown in the Supplemental Information. Upon loading, a clear deflection of the dendrite towards the loading axis is observed. Upon removal of the load, the dendrite turned back towards its original propagation direction. The tendency for dendrites to align with the applied load is consistent with the propagation of a pressurized crack. Continuous metal plating results in a pressure buildup within the metal protrusion. This results in a pressure on the flaw surface (P in Fig. 1b) which drives propagation. Compressive forces (i.e., $\sigma_{applied}$ in Fig. 1c) can act to close cracks, and inhibit propagation perpendicular to the axis of compression. So, under increased load, cracks should turn towards the axis of compression, consistent with the experimental finding in Fig. 2.

At higher applied loads, dendrites deflect into close alignment with the loading axis (Fig. 3). A 30 µm thick electrolyte disc was successively loaded and unloaded as metal dendrites propagated under 0.3 mA/cm^2 galvanostatic current density (Fig. 3a – 3e). In this experiment, applied 200 MPa compressive loads produced dendrite growth nearly aligned with the loading direction, even for current densities up to 5 mA/cm^2 (Figs. 3f – 3j). Upon load removal, the dendrites grow towards the stripping electrode, and eventually electrically short the cell (seen in Fig. 3j). This observation demonstrates that compressive stresses can prevent electrical shorting.

Results for thick electrolyte samples were similar. In Fig. 4, metal filaments in a thicker solid electrolyte disc (250 µm, as compared to 30 µm as in Fig. 3) are also observed to deflect under load. Growing dendrites deflected towards the loading axis (Fig. 4c – 4e), with the crack plane oriented normal to the page (Fig. 4f). This result shows that compressive stresses may be used to mitigate dendrite propagation in electrolyte samples of similar thickness to those commonly studied in literature.

All experiments here showed that compressive stresses impact both the propagation direction and the orientation of metal dendrites in solid electrolytes. The deflection increases with the load's magnitude: a 70 MPa load produced a small deviation in the dendrite propagation direction. Larger applied loads ($\sigma_{applied}$ = 200 MPa) produced dendrite growth nearly parallel to the loading axis. Stated plainly,

compressive loads can deflect metal dendrites to the extent that electrical short-circuiting of the solid electrolyte is completely averted. During preparation of this manuscript, we became aware of a recent pre-print from McConohy, Xu et al.[14], in which a correlation is observed between the strain applied to a solid electrolyte and the initial dendrite growth morphology (at a few micrometer length scale). Those results are qualitatively consistent with the present findings; as we show, regardless of the initial orientation of a growing dendrite, the direction of propagation can be changed by an imposed stress field.

Fracture mechanics model for dendrite deflection

From fracture mechanics, we develop a model to describe the dendrite trajectory under mechanical loading. We will use this model to interpret our experimental results, and later to provide criteria for deflecting dendrites (thus averting electrical shorting). Dendrites are modeled as slit-like metal-filled flaws initially oriented at angle β from the horizontal (Fig. 5a) in a homogeneous and isotropic solid electrolyte. The planar electrolyte/electrode interface is held with fixed x-displacement. Metal plating into the flaw leads to a uniform pressure of P normal to the flaw face. In the absence of any other stresses in the electrolyte, this plating-induced pressure P causes the dendrite to propagate forward without kinking. When an additional load is applied to the solid electrolyte in the vertical direction (σ_{yy}), the energetically preferred path for dendrite propagation is at a kinked angle from its initial orientation,[15,16] as seen in Fig. 5a. The stress state in front of the crack tip crack is then a result of the superposition of the plating-induced pressure and the applied load. The most favorable propagation angle (θ in Fig. 5a) maximizes the local stress intensity factor for an infinitesimal extension of the crack tip. The derivation underlying this model is detailed in Methods.

This model provides a means to assess whether the experimental observations are consistent with fracture-governed dendrite propagation. If filament propagation is driven purely by mechanical fracture, the plating-induced pressure P that would be inferred from experiments would match the fracture stress expected from an *ex-situ* test (called $\sigma_{critical}$). If, on the other hand, propagation is governed largely by chemical degradation, as would be the case for failure via electronic leakage, then the inferred P should be much lower than $\sigma_{critical}$. We estimate $\sigma_{critical}$ by drawing on the analysis of Beuth et al.[17], who studied propagation of through-cracks in a thin plate of the geometry in Fig. 2. Applying their analysis to the 90 μm thick LLZTO disc studied here (detailed further in Methods) yields $\sigma_{critical}$ values between 65 and 120 MPa (for LLZTO fracture toughness, K_{IC}, of 1-2 MPa$\sqrt{m}$)[2,18]. The plating-induced pressure P is independently inferred from the change in filament propagation angle under a known load. From Fig. 2, the measured angles of $\beta = 36°$ and $\theta = 71°$ under an applied load of 70 MPa yield $P = 115$ MPa, which is indeed similar in magnitude to $\sigma_{critical}$. This comparison supports the conclusion that dendrite propagation is a fracture process in which the plating-induced pressure P is approximately the critical stress required for fracture.

The model results capture key aspects of experimental behavior, and provide design criteria for averting failure. The results in Fig. 5 show that in-plane stresses slightly larger than P should deflect dendrites of any initial orientation, β, to a final angle $\theta = 90°$, thereby averting cell shorting. Figure 5b plots the most energetically favorable propagation angle as a function of the load (given as σ_{yy}/P) and the initial crack inclination, β. For a given β, compressive σ_{yy} increases the propagation angle θ for all β (consistent with Fig. 2), whereas tensile σ_{yy} decreases β. A critical stress exists for reaching the design objective $\theta = 90°$. For some range of $\theta < 90°$, short-circuiting may still be avoided depending on the thickness and lateral dimensions of the solid electrolyte. However, for compressive stress, θ is always larger than β until β reaches 90°. Note that a relatively small overstress provides a substantial margin of safety; Fig. 5c shows that a compressive stress only 10% larger than P (i.e., $\sigma_{yy} \approx 1.1P$) forces $\theta = 90°$

for all initial angles β. This result is consistent with the experimental observation (Figs. 3 – 4) that a 200 MPa load repeatedly deflects all observed filaments to $\theta \approx 90°$. In the following section, we model the critical stress and corresponding engineering requirements for dendrite deflection in solid-state battery architectures.

Engineering solid-state batteries for dendrite deflection

The insights described above are transferable to realistic solid-state battery architectures. Beyond externally applied stresses, the required in-plane stresses necessary to deflect dendrites can be produced by other means. As one example, we show that thermal expansion mismatches are easily capable of producing the desired in-plane residual stresses within layers of a prototypical solid-state lithium battery in which the solid-electrolyte layer is bounded by a lithium metal negative electrode and an oxide cathode (Fig. 6a). Assuming no delamination between the Li – solid electrolyte and solid electrolyte – cathode interfaces, a thermal expansion mismatch between layers will result in a residual stress. However, the very low yield stress of Li metal (~1 MPa[19–21]) indicates that it will flow to relieve the resulting stress. On the other hand, a non-ductile solid electrolyte and cathode will support thermal expansion mismatch stresses. To achieve high energy density and fast charging, it is furthermore desirable that the electrolyte be thin relative to the cathode. In this case, the residual stress will be primarily borne by the solid electrolyte, as desired. If the cathode has a higher coefficient of thermal expansion than the electrolyte, the electrolyte will experience a residual compressive stress after cooling from the stress-free state at elevated temperature. An alternate approach to producing the requisite compressive biaxial stress in a solid-electrolyte layer is to laminate two solid-electrolytes with different thermal expansion coefficients (Fig. 6a), in which case the electrolyte of lower α receives the compressive stress. In both cases, the residual compressive stress is expressed as:

$$\sigma = E'\varepsilon_{th} = E'\Delta\alpha\Delta T$$

where σ is the in-plane stress (σ_{yy} from the right side of Fig. 5a) at the cathode-electrolyte interface, E' is the electrolyte biaxial elastic modulus, ε_{th} is the strain induced by the cathode / electrolyte thermal expansion mismatch, $\Delta\alpha$ is the difference in thermal expansion coefficients of the anode-facing material and its counterpart. If there is no mechanical relaxation (i.e., bending, creep, or interfacial delamination), then the resulting residual compression will act to deflect dendrites just as P in Fig. 5. From the analysis in the previous section, P can be taken as $\sigma_{crit.}(\approx \frac{K_{IC}}{1.12\sqrt{\pi a}}$ for this loading condition, with K_{IC} and a as 1 MPa$\sqrt{m}$ and 10 μm).

Figure 6b lists biaxial moduli and thermal expansion coefficient values for several lithium ion cathodes and electrolytes. Notice that LiFePO$_4$ (LFP)[22] has a higher α than the three widely-studied solid electrolytes listed (LLZTO[23], Li$_{10}$GeP$_2$S$_{12}$ (LGPS)[24,25] and Li$_{1+x}$Al$_x$Ti$_{2-x}$(PO$_4$)$_3$ (LATP)[26,27]). Plotted in Fig. 6c are lines of thermal residual stress vs processing temperature (assuming a quench to T$_1$=20°C) for several solid electrolyte – cathode and solid electrolyte – solid electrolyte pairs. The horizontal dashed line demarks the compressive stress of 150 MPa required for complete dendrite deflection. The processing temperature values are upper bounds since they are calculated assuming fully-dense solids and no plastic deformation under stress. Nonetheless, it is seen that a modest quench can reach the threshold residual compressive stress of 150 MPa, only 50°C to 60°C for LATP and LLZO vs LFP, and ~60°C for LATP and LLZO vs LGPS. Thermal cycles of this magnitude are readily incorporated into electrolyte fabrication techniques producing dense electrolytes which reach maximum temperatures of 100-300°C[28]. On the other hand, for some materials combinations, a much larger temperature excursion is necessary, and may be difficult to achieve. Figure 6c shows that the threshold stress is reached for a quench of

4

350°C for LiPON against LLZO, 550°C for LGPS against LFP, and 1220°C for LATP against NMC. The results shown here are readily modified for alternative cell architectures and other materials, including composite electrolytes[29–32](e.g. co-sintered cathodes / electrolytes, Fig. 6a). The model predicts that only three parameters, E', $\Delta\alpha$, and ΔT, are required to determine a critical compressive stress such as 150 MPa.

Deleterious effects of stack pressure on dendrite propagation

A stack pressure (σ_{xx}, Fig. 5a) has been widely used in previous studies, and is observed to increase critical current densities and improve the uniformity of metal deposition. Stack pressures commonly vary from a few to several hundred MPa.[31,33–37] A previously unrecognized result, highlighted by Fig. 5d, is that stack pressure is predicted by our model to have a deleterious effect by directing dendrite growth towards the electrode, promoting short-circuiting.[38] Figure 5d shows that, up to several times P, increasing stack pressures tend to decrease the propagation angle θ and ensure that dendrites will take a direct (rather than tortuous) path to penetrating the cell.

Conclusions

We propose a stress-based approach to mitigating metal dendrite failure in solid state batteries. Using experiments and a fracture mechanics model, we show that metal dendrites growing through solid electrolyte can be deflected by an imposed stress. For Li metal dendrites growing in LLZTO electrolyte, a compressive in-plane stress is observed to deflect the dendrite growth trajectory away from the electric field lines towards the compressive loading axis. The experiment and model show that regardless of the initial orientation of a growing dendrite, a critical stress of ~150 MPa applied orthogonally to the electric field vector can deflect growing dendrites sufficiently to avoid short circuits. This insight is used to propose materials combinations and processing approaches wherein residual stresses resulting from thermal expansion mismatch could be used to produce desirable stresses in laminate solid state battery architectures.

The results here also help to resolve an existing controversy as to whether metal dendrite growth is dominated by fracture or by internal reduction of lithium ions to lithium metal. Since the experiments are conducted under conditions where dendrite growth due to internal reduction of lithium ions remains possible, yet no evidence of such growth occurs when stress-deflection is active, it is concluded that, at least for the materials tested here, metal dendrite growth proceeds by mechanical fracture rather than electronic conduction based internal Li$^+$ reduction.

Acknowledgements

Author contributions

CDF and YMC conceptualized the study. CDF designed and executed the experiments, and analyzed the data with input from all authors. CDF developed the mixed-mode fracture model with input from CG, WCC, and BS. YMC and CDF developed the concepts for internally stressed batteries. CDF wrote the first draft of the manuscript.

Methods

Cell preparation and assembly

Polycrystalline LLZTO was obtained from Toshima Manufacturing Inc. (Saitama, Japan) as 1 mm thick, 12.7 mm diameter pellets. The phase purity of these pellets was confirmed via X-ray diffraction, and the bulk conductivity was measured as 1.03 mS/cm in the previous work of Park et al.[2] LLZTO electrolytes were then mechanically polished to the end thickness specified within the text, using oil-based 1 μm diamond suspension for the last polishing step. Immediately after polish, the electrolyte discs were transferred into an oven within an Ar-containing glovebox. The discs were heat treated at 500°C for 3 hours.

The Li metal / LLZTO interface was formed using similar methods to previous works[2,10]. Specifically, after heat treatment, the electrolyte discs were removed from the oven. Li metal foil (Alfa Aesar, Ward Hill, Massachusetts, USA) was scraped with a steel spatula to produce a clean metal surface. This Li was then cut into 3 mm diameter pads using a biopsy punch. The Li metal pads were immediately adhered to the LLZTO disk, and the resulting assembly was placed into the oven and baked at 250°C for 1 hour.

The resulting plan-view cells were fixed to a cantilever bar using Loctite 401 adhesive. For the experiment shown in Fig. 3a, a 1/8" thick, 1" wide, 2' long 6061 aluminum bar (McMaster, Elmhurst, Illinois, United States) was used. All other experiments used 1/2" thick, 1" wide, 2' long acrylic bars (McMaster, Elmhurst, Illinois, United States). A strain gauge was fixed to the cantilever in a manner identical to the cell. The adhesive was allowed to cure for 3 hours. Following this, the bar was fixed to a rigid frame as shown in Fig. 1. The cell and strain gauge were located approximately 18" from the free end of the cantilever. Tungsten probe tips were inserted into the Li metal electrodes so as to provide an electrical connection to a VMP-3 Potentiostat (Biologic, Knoxville, Tennessee, USA). This electrical connection permitted controlled electrochemical cycling within the glovebox.

Operando measurements

Operando optical measurements were recorded using a Leica DMS300 microscope, with the sample backlit using an LED plate. Electrochemical cycling and measurement were conducted using a VMP-3 Potentiostat (Biologic, Knoxville, Tennessee, USA). All currents discussed in the text were applied to the cell galvanostatically, with the current density representing the applied current divided by the initial Li electrode area.

Meanwhile, strain measurements were collected from a strain gauge (CEA-06-250UN-350/P2, Micro-Measurements, Raleigh, North Carolina, USA) fixed adjacent to the cell. Strain data (ε_{gauge}) was collected in real time using a D4 Data acquisition system (Micro-Measurements, Raleigh, North Carolina, USA). The distance from the end of the bar for both the sample (L_{elyte}) and the strain gauge (L_{gauge}) are measured using a ruler. Because the gauge and the sample are positioned at different distances from the end of the bar, they possess slightly different strains. Thus, the strain in the electrolyte can be estimated by correcting the strain in the gauge using beam bending theory. From Euler-Bernoulli beam bending theory,[39] the axial strain at a point on the surface of the cantilever can be written as

$$\varepsilon = \frac{6WL}{E_{cantilever}bh^3}$$

With W as the weight applied to the free end of the cantilever, L as the distance from the end of the cantilever, b as the length of the cantilever's base, and h as the height of the cantilever. From the above equation, we know that (for a constant load) the value of ε/L is constant everywhere on the bar. In testing, holding a test cantilever and gauge loaded for a period of several hours did not yield a significant change in the measured strain. Therefore, we can conclude that the gauge and the sample are rigidly fixed to the cantilever. Thus, the average strain in the electrolyte (ε_{elyte}) is related to the measured strain in the gauge by

$$\frac{\varepsilon_{elyte}}{L_{elyte}} = \frac{\varepsilon_{gauge}}{L_{gauge}} \rightarrow \varepsilon_{elyte} = \varepsilon_{gauge}\left(\frac{L_{elyte}}{L_{gauge}}\right)$$

The electrolyte strain along the cantilever's axis was calculated from the measured strain based upon the above equation. Given that the radius r_{elyte} of the electrolyte (0.25") is very small compared to the distance from the end of the bar (~18"), the strain state differs minimally at the edges of the electrolyte as compared to the center of the electrolyte ($\varepsilon_{elyte\ edges} = \frac{L_{elyte} \pm r_{elyte}}{L_{elyte}} = (1 \pm 0.014)\varepsilon_{elyte}$). Because the electrolyte is very thin compared to the cantilever, the cantilever effectively prevents the electrolyte from straining perpendicular to the bar's axis. Thus, other strains within the plane of the bar's surface can be neglected, yielding a plane strain elastic problem. From Hooke's law, we can state the stress along the bar's axis ($\sigma_{applied}$) as:

$$\sigma_{applied} = \frac{E_{LLZTO}}{1 - \nu^2}\varepsilon_{elyte}$$

The measured stresses reported within the main text and supplementary information are then reported as $\sigma_{applied}$ while taking E_{LLZTO} and ν LLZTO as 150 GPa and 0.25, respectively[40].

Predicting kink angle from mixed mode fracture mechanics

The maximum strain energy release rate for a crack at angle $90° - \beta$ from the direction of a normal load occurs at the kink angle α which maximizes the local mode I stress intensity factor k, defined as[41]:

$$k_I(\alpha) = C_{11}K_I + C_{12}K_{II} \tag{1}$$

Where K_I and K_{II} are the stress intensity factors for mode I and mode II such that

$$K_I = K_{I(0)}\cos^2\beta \tag{2}$$
$$K_{II} = K_{I(0)}\cos\beta\sin\beta \tag{3}$$

Where $K_{I(0)}$ represents the stress intensity factor if the crack was at $\beta = 0$. Taking the prefactor and crack length as unity yields:

$$K_{I(0)} = \sigma \tag{4}$$

With σ as the applied load, and where C_{11}, C_{12} are coefficients such that:

$$C_{11}(\alpha) = \frac{3}{4}\cos\left(\frac{\alpha}{2}\right) + \frac{1}{4}\cos\left(\frac{3\alpha}{2}\right) \tag{5}$$

$$C_{12}(\alpha) = -\frac{3}{4}\left[\sin\left(\frac{\alpha}{2}\right) + \sin\left(\frac{3\alpha}{2}\right)\right] \tag{6}$$

With α being the angle of the kink from the plane of the crack.

In the problem of interest, we have two applied stresses, which can be superimposed to predict the kink angle for a growing crack: 1) A plating-induced mode I load P of unit pressure and 2) an applied normal (compressive) load of $\hat{\sigma} = \frac{\sigma_{applied}}{P}$ aligned with the bar's axis, acting upon a crack oriented at angle $90° - \beta$. This second load represents the external compression on the electrolyte. The plating-induced pressure is applied normal to the crack faces, and oriented at an angle of β relative to the coordinate system of load 2. Thus, the remotely applied stress state can be described using superposition as:

$$R(\beta)\begin{bmatrix} 0 & 0 \\ 0 & 1 \end{bmatrix}R^T(\beta) + \begin{bmatrix} -\nu\hat{\sigma} & 0 \\ 0 & -\hat{\sigma} \end{bmatrix} = \begin{bmatrix} \sigma_{xx} & \sigma_{xy} \\ \sigma_{xy} & \sigma_{yy} \end{bmatrix} \tag{7}$$

Where R is the rotation matrix:

$$R(\theta) = \begin{bmatrix} \cos\theta & -\sin\theta \\ \sin\theta & \cos\theta \end{bmatrix} \tag{8}$$

This system can be rotated by an angle θ' to give the principle stress state, such that

$$R(\theta' + \beta)\begin{bmatrix} 0 & 0 \\ 0 & 1 \end{bmatrix}R^T(\theta' + \beta) + R(\theta')\begin{bmatrix} -\nu\hat{\sigma} & 0 \\ 0 & -\hat{\sigma} \end{bmatrix}R(\theta') = \begin{bmatrix} \sigma_1 & 0 \\ 0 & \sigma_2 \end{bmatrix} \tag{9}$$

Where σ_1 and σ_2 are the principle stresses, with $\sigma_1 > \sigma_2$. The exact values of σ_1, σ_2, and θ' are determined by the eigenvalues and eigenvectors of the initial system for a given value of $\hat{\sigma}$ and β. This allows for the determination of the local stress intensity factor by superimposing two principle stresses at $90°$ to one another, permitting equations 2, 3, and 4 to be rewritten:

$$K_I = [\sigma_1 \cos^2(\beta - \theta') + \sigma_2 \sin^2(\beta - \theta')] \tag{10}$$

$$K_{II} = [(\sigma_1 - \sigma_2)\sin(\beta')\cos(\beta - \theta')] \tag{11}$$

The most energetically favorable kink angle, α^*, is then defined as the angle α that maximizes the local stress intensity factor, k_I, now rewritten from equation 1, 10, and 11 as:

$$k_I(\alpha) = \tag{12}$$
$$C_{11}(\alpha)[\sigma_1 \cos^2(\beta - \theta') + \sigma_2 \sin^2(\beta - \theta')] + C_{12}(\alpha)[(\sigma_1 - \sigma_2)\sin(\beta - \theta')\cos(\beta - \theta')]$$

We determine this optimum angle α^* numerically. Because this kink angle is relative to the initial crack orientation, the direct sum of the most favorable kink angle α^* to the crack angle β yields the ultimate propagation angle $\theta = \alpha^* + \beta$ discussed in the text.

We note that this analysis considers only the most favorable angle of dendritic propagation, which is directly relevant to the amount of material that must be plated prior to failure. A smaller

propagation angle implies that more metal plating must occur before dendrite-induced shorting, while a larger angle implies the opposite. However, this analysis does not directly consider the exact value of the driving force after the crack kinks, nor does it investigate the impact of the electric field on propagation. Furthermore, we have assumed the electrolyte to be isotropic and homogeneous. In reality, electrolytes possess microstructural features and defects which may impact the mechanics and thus morphology of propagating flaws.

In the above analysis, the kink angle possesses no direct dependence on flaw size. For a channel crack in a thin film, the critical pressure for fracture possesses no flaw length dependence, so long as the flaw is substantially longer than the film thickness. This greatly simplifies analysis of the plan-view cells outlined here. For a conventional cell format, an indirect dependence on flaw size occurs via the dependence of P on the flaw size. In applying this analysis to conventional cells, we must assume a representative flaw size and stress intensity factor for failure to estimate a representative P. As discussed in the main text, we use $a = 10\mu m$ and $K_c = 1\ MPa \cdot \sqrt{m}$. We note that for flaws initially smaller than the representative 10 μm used here, the initial value of P is higher. However, with propagation, the value of P decreases until reaching that of the representative flaw discussed here. Thus, the analysis outlined herein should still apply.

Estimating the mechanical pressure to propagate a channel crack in a thin film

We estimate the mechanical pressure to propagate a channel crack in an LLZTO film on the cantilever substrate, as shown in Fig. 3a. We treat the dendrite shown in Fig. 3a as a channel crack propagating through a thin film bonded to a semi-infinite elastic substrate. Both the film and the substrate are treated as isotropic, homogeneous, linear elastic materials with known Young's modulus E and Poisson ratio v. Treating this cracking as a plane strain problem, the material dependence depends on the two dimensionless parameters α_d and β_d (the Dundurs parameters)[17], such that

$$\alpha_d = \frac{\bar{E}_{film} - \bar{E}_{sub.}}{\bar{E}_{film} + \bar{E}_{sub}} \qquad \beta_d = \frac{\mu_{film}(1 - 2v_{sub.}) - \mu_{sub.}(1 - 2v_{film})}{2\mu_{film}(1 - v_{sub.}) + 2\mu_{sub.}(1 - v_{film})}$$

Where $\bar{E}$ is the plane strain modulus, $\bar{E} = E/(1 - v^2)$, and μ is the shear modulus, $\mu = 2E/(1 + v)$. The only two length scales present in this problem are the film thickness and the crack length. According to Nakamura and Kamath[42], in the limit that the crack length is larger than the film thickness, the strain energy release rate (and thus stress intensity factor) is independent of crack length. This allows us to invoke the analysis from Beuth[17] to estimate the steady state energy release rate ($G_{ss.}$) for a uniform stress σ on the crack face:

$$G_{ss.} = g(\alpha_d, \beta_d)\frac{\pi}{2}\frac{\sigma^2 t_{film}}{\bar{E}_{film}}$$

Where g is a function of the Dundurs parameters outlined by Beuth, and t_{film} is the film thickness. For crack propagation, this strain energy release rate must be equal to the critical strain energy release rate for fracture (Γ), which can be related to measured K[1C] values as follows:

$$\Gamma = \frac{K_{1C}^2}{\bar{E}_{film}} = g(\alpha_d, \beta_d)\frac{\pi}{2}\frac{\sigma_{crit.}^2 t_{film}}{\bar{E}_{film}}$$

Thus, solving for the critical stress $\sigma_{crit.}$ yields:

$$\sigma_{crit.} = \sqrt{\frac{1}{g(\alpha_d, \beta_d)} \frac{2}{\pi} \frac{K_{1C}^2}{t_{film}}}$$

In modelling the LLZTO film, we take $E_{film} = 150$ GPa and $\nu = 0.25$ as from Yu et al.[40] Meanwhile, we consider the elastic properties of the cantilever (6061 Aluminum for Fig. 3a) as $E_{sub.} = 70\ GPa$ and $\nu = 0.25$. These material properties yield Dundurs parameters of $\alpha_d = 0.36$ and $\beta_d = 0.04$, where $g(\alpha_d = 0.36, \beta_d = 0.04) = 1.74$. The LLZTO film shown in Fig. 3a was measured as $90\mu m$ using an optical microscope (BA 310 met, Motic, Barcelona, Spain) with 50x objective. The actual K_{1C} (based upon indentation fracture toughness measurements[2,18]) appears to vary between $1 - 2$ MPa$\sqrt{m}$, as would be expected for a brittle ceramic. Taking 1 and 2 MPa$\sqrt{m}$ as upper and lower bounds produces $\sigma_{crit.}$ between 65 and 120 MPa$\sqrt{m}$.

References

1.   Albertus, P., Babinec, S., Litzelman, S. & Newman, A. Status and challenges in enabling the lithium metal electrode for high-energy and low-cost rechargeable batteries. *Nature Energy* **3**, 16–21 (2018).

2.   Park, R. J.-Y. *et al.* Semi-solid alkali metal electrodes enabling high critical current densities in solid electrolyte batteries. *Nature Energy* **6**, 314–322 (2021).

3.   Han, F. *et al.* High electronic conductivity as the origin of lithium dendrite formation within solid electrolytes. *Nat Energy* **4**, 187–196 (2019).

4.   Armstrong, R. D., Dickinson, T. & Turner, J. The breakdown of β-alumina ceramic electrolyte. *Electrochimica Acta* **19**, 187–192 (1974).

5.   De Jonghe, L. C., Feldman, L. & Beuchele, A. Slow degradation and electron conduction in sodium/beta-aluminas. *Journal of Materials Science* **16**, 780–786 (1981).

6.   Liu, X. *et al.* Local electronic structure variation resulting in Li 'filament' formation within solid electrolytes. *Nat. Mater.* **20**, 1485–1490 (2021).

7.   Zhao, J. *et al.* In situ Observation of Li Deposition-Induced Cracking in Garnet Solid Electrolytes. *ENERGY & ENVIRONMENTAL MATERIALS* **5**, 524–532 (2022).

8.   Porz, L. *et al.* Mechanism of lithium metal penetration through inorganic solid electrolytes. *Advanced Energy Materials* **7**, 1701003 (2017).

9.   Sharafi, A., Meyer, H. M., Nanda, J., Wolfenstine, J. & Sakamoto, J. Characterizing the Li–Li7La3Zr2O12 interface stability and kinetics as a function of temperature and current density. *Journal of Power Sources* **302**, 135–139 (2016).

10.   Kazyak, E. *et al.* Li Penetration in Ceramic Solid Electrolytes: Operando Microscopy Analysis of Morphology, Propagation, and Reversibility. *Matter* **2**, 1025–1048 (2020).

11.   Swamy, T. *et al.* Lithium metal penetration induced by electrodeposition through solid electrolytes: example in single-crystal Li6La3ZrTaO12 garnet. *Journal of the Electrochemical Society* **165**, A3648 (2018).

12.   Ning, Z. *et al.* Visualizing plating-induced cracking in lithium-anode solid-electrolyte cells. *Nat. Mater.* **20**, 1121–1129 (2021).

13.   Qi, Y., Ban, C. & Harris, S. J. A New General Paradigm for Understanding and Preventing Li Metal Penetration through Solid Electrolytes. *Joule* **4**, 2599–2608 (2020).

14.   McConohy, G. *et al. ChemRxiv* doi:10.26434/chemrxiv-2022-332l0.

15.   Williams, J. G. & Ewing, P. D. Fracture under complex stress—the angled crack problem. *International Journal of Fracture Mechanics* **8**, 441–446 (1972).

16.   Cotterell, B. & Rice, Jr. Slightly curved or kinked cracks. *International journal of fracture* **16**, 155–169 (1980).

17.   Beuth Jr, J. L. Cracking of thin bonded films in residual tension. *International Journal of Solids and Structures* **29**, 1657–1675 (1992).

18.   Wolfenstine, J. *et al.* A preliminary investigation of fracture toughness of Li7La3Zr2O12 and its comparison to other solid li-ionconductors. *Materials letters* **96**, 117–120 (2013).

19.   Fincher, C. D., Ojeda, D., Zhang, Y., Pharr, G. M. & Pharr, M. Mechanical properties of metallic lithium: from nano to bulk scales. *Acta Materialia* **186**, 215–222 (2020).

20.   LePage, W. S. *et al.* Lithium mechanics: roles of strain rate and temperature and implications for lithium metal batteries. *Journal of The Electrochemical Society* **166**, A89 (2019).

21.   Masias, A., Felten, N., Garcia-Mendez, R., Wolfenstine, J. & Sakamoto, J. Elastic, plastic, and creep mechanical properties of lithium metal. *Journal of materials science* **54**, 2585–2600 (2019).

22.   Kim, S., Wee, J., Peters, K. & Huang, H.-Y. S. Multiphysics coupling in lithium-ion batteries with reconstructed porous microstructures. *The Journal of Physical Chemistry C* **122**, 5280–5290 (2018).

23.   Hubaud, A. A., Schroeder, D. J., Ingram, B. J., Okasinski, J. S. & Vaughey, J. T. Thermal expansion in the garnet-type solid electrolyte (Li7− xAlx/3) La3Zr2O12 as a function of Al content. *Journal of Alloys and Compounds* **644**, 804–807 (2015).

24.   Weber, D. A. *et al.* Structural Insights and 3D Diffusion Pathways within the Lithium Superionic Conductor Li10GeP2S12. *Chem. Mater.* **28**, 5905–5915 (2016).

25.   Deng, Z., Wang, Z., Chu, I.-H., Luo, J. & Ong, S. P. Elastic Properties of Alkali Superionic Conductor Electrolytes from First Principles Calculations. *J. Electrochem. Soc.* **163**, A67–A74 (2016).

26.   Yan, G. *et al.* Influence of sintering temperature on conductivity and mechanical behavior of the solid electrolyte LATP. *Ceramics international* **45**, 14697–14703 (2019).

27.   Jackman, S. D. & Cutler, R. A. Effect of microcracking on ionic conductivity in LATP. *Journal of Power Sources* **218**, 65–72 (2012).

28.   Kim, K. J., Balaish, M., Wadaguchi, M., Kong, L. & Rupp, J. L. Solid-state Li–metal batteries: challenges and horizons of oxide and sulfide solid electrolytes and their interfaces. *Advanced Energy Materials* **11**, 2002689 (2021).

29.   Hitz, G. T. *et al.* High-rate lithium cycling in a scalable trilayer Li-garnet-electrolyte architecture. *Materials Today* **22**, 50–57 (2019).

30.   Fu, K. (Kelvin) *et al.* Three-dimensional bilayer garnet solid electrolyte based high energy density lithium metal–sulfur batteries. *Energy Environ. Sci.* **10**, 1568–1575 (2017).

31.   Ye, L. & Li, X. A dynamic stability design strategy for lithium metal solid state batteries. *Nature* **593**, 218–222 (2021).

32.   Sastre, J. *et al.* Blocking lithium dendrite growth in solid-state batteries with an ultrathin amorphous Li-La-Zr-O solid electrolyte. *Communications Materials* **2**, 1–10 (2021).

33.   Krauskopf, T., Hartmann, H., Zeier, W. G. & Janek, J. Toward a fundamental understanding of the lithium metal anode in solid-state batteries—an electrochemo-mechanical study on the garnet-type solid electrolyte Li6. 25Al0. 25La3Zr2O12. *ACS applied materials & interfaces* **11**, 14463–14477 (2019).

34.   Krauskopf, T., Mogwitz, B., Rosenbach, C., Zeier, W. G. & Janek, J. Diffusion Limitation of Lithium Metal and Li–Mg Alloy Anodes on LLZO Type Solid Electrolytes as a Function of Temperature and Pressure. *Advanced Energy Materials* **9**, 1902568 (2019).

35. Doux, J.-M. *et al.* Stack pressure considerations for room-temperature all-solid-state lithium metal batteries. *Advanced Energy Materials* **10**, 1903253 (2020).

36. Meyer, A., Xiao, X., Chen, M., Seo, A. & Cheng, Y.-T. A Power-Law Decrease in Interfacial Resistance Between Li7La3Zr2O12 and Lithium Metal After Removing Stack Pressure. *Journal of The Electrochemical Society* **168**, 100522 (2021).

37. Doux, J.-M. *et al.* Pressure effects on sulfide electrolytes for all solid-state batteries. *Journal of Materials Chemistry A* **8**, 5049–5055 (2020).

38. Poisson constraints may result in a decreased stress intensity factor for a laterally constrained stack, but this effect is not sufficient to prevent dendrite growth under any reasonable electrical potential.

39. Gere, J. M. & Timoshenko, S. P. Mechanics of Materials. ed. *Boston, MA: PWS* (1997).

40. Yu, S. *et al.* Elastic properties of the solid electrolyte Li7La3Zr2O12 (LLZO). *Chemistry of Materials* **28**, 197–206 (2016).

41. Anderson, T. L. *Fracture mechanics: fundamentals and applications*. (CRC press, 2017).

42. Nakamura, T. & Kamath, S. M. Three-dimensional effects in thin film fracture mechanics. *Mechanics of Materials* **13**, 67–77 (1992).

43. Athanasiou, C. E. *et al.* Rate-dependent deformation of amorphous sulfide glass electrolytes for solid-state batteries. *Cell Reports Physical Science* **3**, 100845 (2022).

44. Athanasiou, C. E., Jin, M. Y., Ramirez, C., Padture, N. P. & Sheldon, B. W. High-toughness inorganic solid electrolytes via the use of reduced graphene oxide. *Matter* **3**, 212–229 (2020).

45. Cheng, E. J. *et al.* Mechanical and physical properties of LiNi0. 33Mn0. 33Co0. 33O2 (NMC). *Journal of the European Ceramic Society* **37**, 3213–3217 (2017).

46. Lee, E. *et al.* Tracking the Influence of Thermal Expansion and Oxygen Vacancies on the Thermal Stability of Ni-Rich Layered Cathode Materials. *Adv. Sci.* **7**, 1902413 (2020).

47. Dang, S. O. *Modelling Thermodynamic Properties of Intercalation Compounds for Lithium Ion Batteries*. (Werkstoffstruktur und-eigenschaften, 2016).

48. Hoffart, L. & Schleich, D. M. Morphological Investigations on the Solid Electrolyte Li3.6Geo.6Vo.404 and Use in a Solid State Lithium Battery. 6 (1995).

49. Vereda, F. *et al.* A study of electronic shorting in IBDA-deposited Lipon films. *Journal of Power Sources* **89**, 201–205 (2000).

50. Herbert, E. G., Tenhaeff, W. E., Dudney, N. J. & Pharr, G. M. Mechanical characterization of LiPON films using nanoindentation. *Thin Solid Films* **520**, 413–418 (2011).
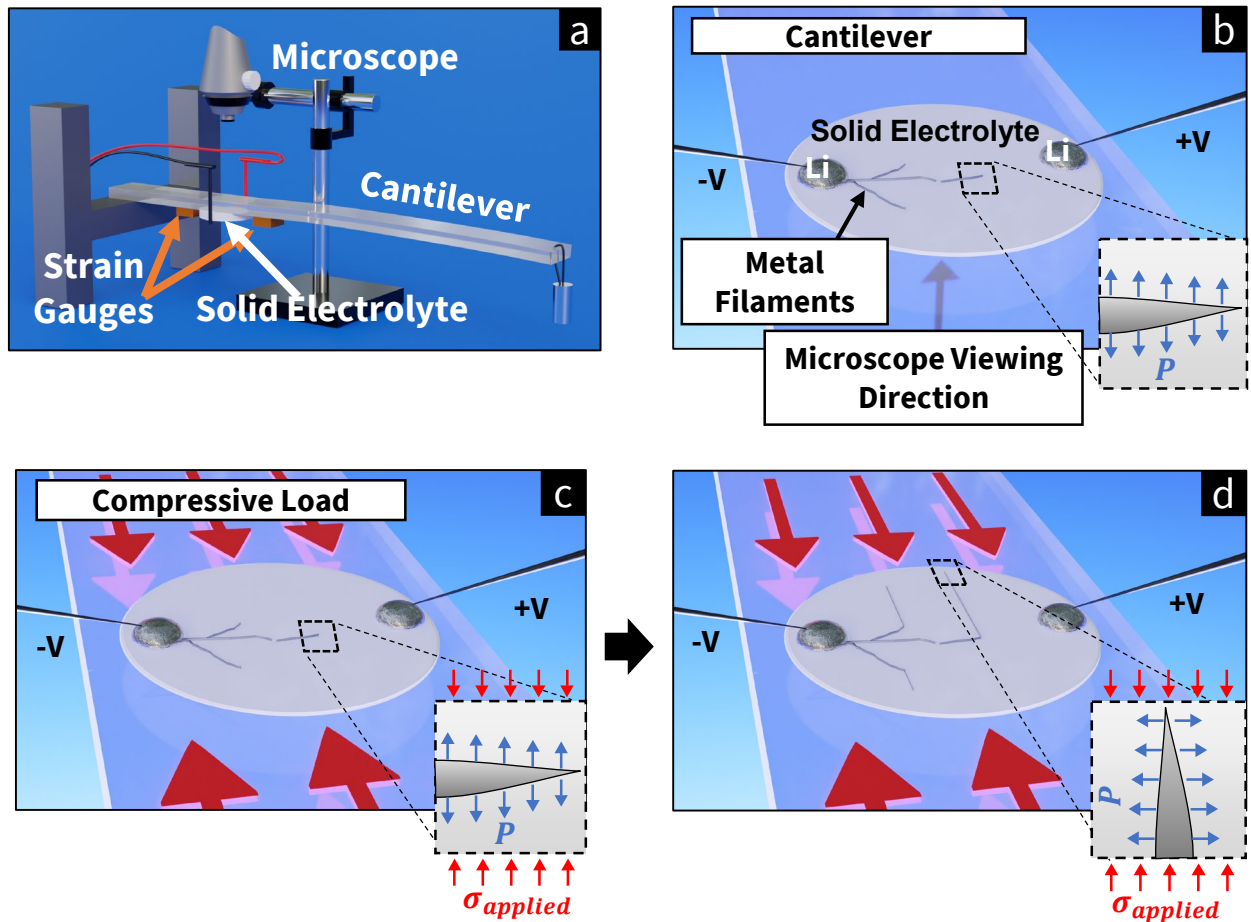
Fig. 1: Observing the response of metal dendrites to applied loads.

a) A microscope observes a solid state cell consisting of lithium metal electrodes adhered to a thin solid electrolyte plate (1/2" diameter), fixed rigidly to a transparent cantilever. Weight applied to the end of the cantilever induces strain in the bar and the electrolyte. This strain is measured in real time using strain gauges.

b) The plan-view cell geometry and dendrite orientation in the load-free configuration. Applied current produces plating-induced pressure (P) inside metal-filled flaws at the anode / electrolyte interface. This pressure acts normally to the flaw surface, wedging open the flaw and allowing metal dendrites to propagate through the cell.

c) The cell under load. Weight placed on the end of the cantilever (see (a)) generates compressive strains in the cantilever and the electrolyte. Resulting compressive stress ($\sigma_{applied}$) acts along the cantilever's axis, and opposes the plating-induced pressure P causing crack opening and dendrite propagation.

d) Dendrite deflection when propagating under compressive load. For $\sigma_{applied}$ = 200 MPa, the metal propagation direction turned about 90° to align with the loading axis.
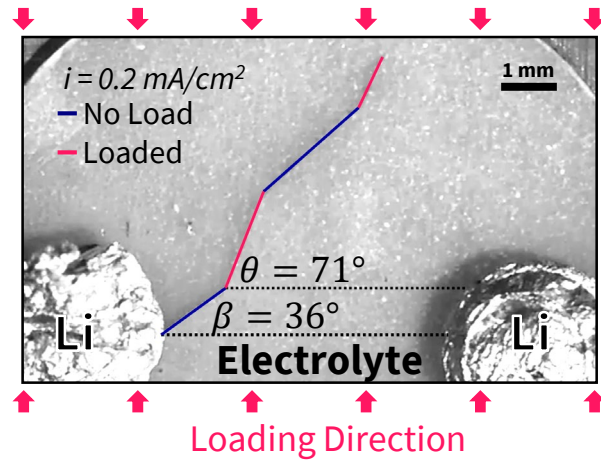
Fig. 2: The response of a metal dendrite to electrochemical and mechanical loadings.

Deflection of a propagating dendrite in response to load. Initially, the dendrite propagates along the segment highlighted in blue under galvanostatic conditions (0.2 mA/cm²). Upon application of 70 MPa compressive stress, deflection of the dendrite along the first red segment occurred. Load removal, and reloading, produced the second blue and red segments, respectively. Image recorded while viewing through the cantilever (viewing direction opposite to that in Fig. 1b); solid-electrolyte is 90 μm thick. All plating occurred at voltages within the LLZTO electrolyte window (voltage and current data available in the Supplementary Information).
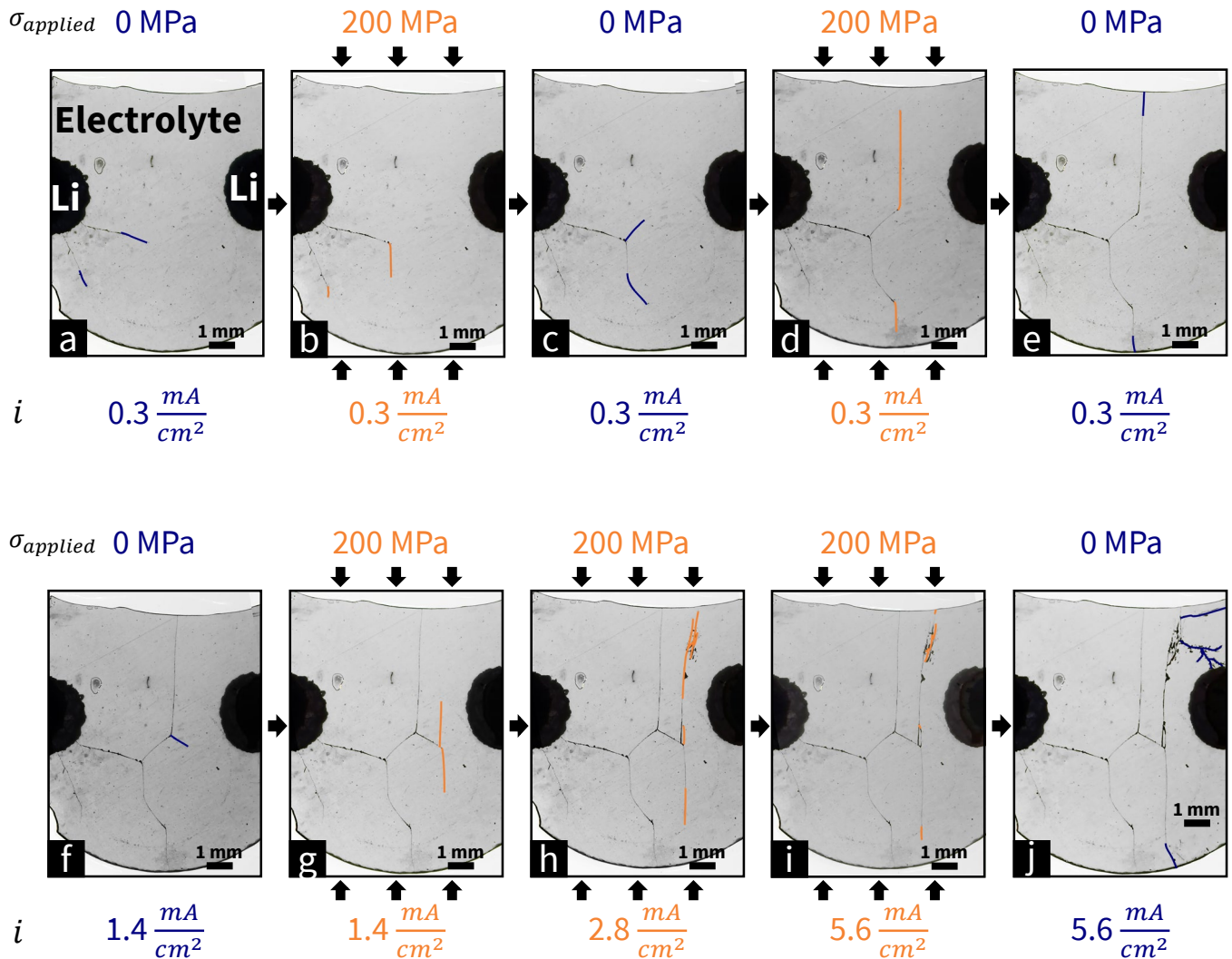
Fig. 3: The response of propagating metal dendrites to applied loads in a 30 μm thick electrolyte, imaged via *operando* microscopy: Metal dendrites initiated at 1.1 mA/cm² galvanostatic current density using the cell configuration from Fig. 1. Dendrite growth-segments are highlighted in each frame. The sequence a – j is chronological. All plating occurred at voltages within the LLZTO electrolyte stability window (voltage and current data available in the Supplementary Information).

a – e)   Metal dendrites propagating under 0.3 mA/cm² galvanostatic current density: the compressive stress in b and d resulted in dendrite growth nearly aligned with the loading direction. When plating occurred without applied loads in a and c, dendrites propagated toward the counter-electrode. For the growth shown in e, the dendrites propagated towards the electrolyte edges, where the dendrites appeared to arrest.

f – j)   Dendrite growth spurred by increasingly high current densities: once the load was re-applied, dendrites grew towards loading direction, even at increasing current-densities as seen in g – i up to 5.6 mA/cm². After the load was removed, metallic dendrites grew towards the stripping electrode and subsequently electrically shorted the cell (seen in j).
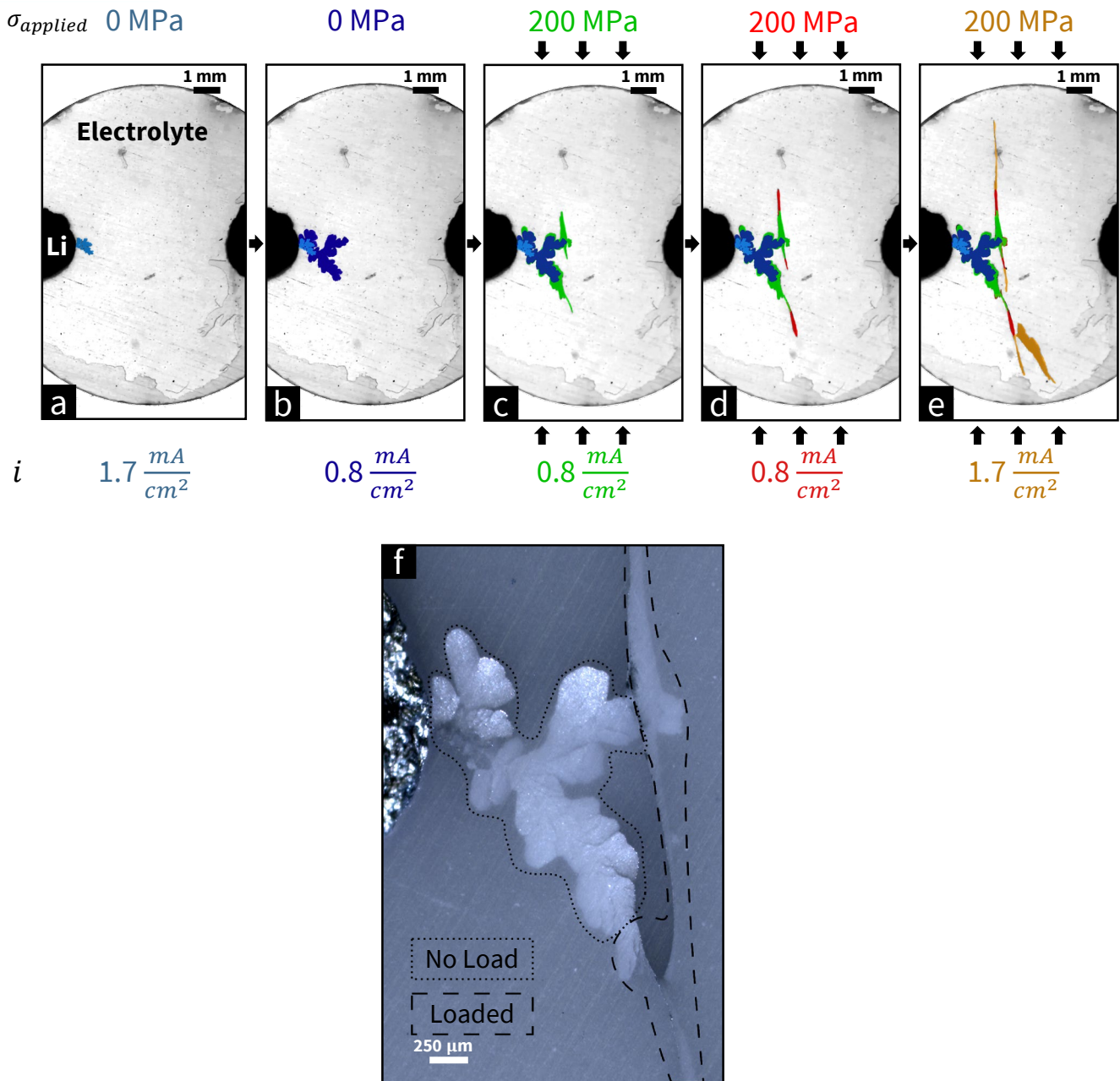
$\sigma_{applied}$ 0 MPa   0 MPa   200 MPa   200 MPa   200 MPa

i $1.7 \frac{mA}{cm^2}$ $0.8 \frac{mA}{cm^2}$ $0.8 \frac{mA}{cm^2}$ $0.8 \frac{mA}{cm^2}$ $1.7 \frac{mA}{cm^2}$

Fig. 4: The response of propagating metal dendrites to applied loads in a 250 μm thick electrolyte.

Metal dendrites initiated at 1.7 mA/cm^2 galvanostatic current density using the cell geometry shown in Fig. 1. Fig. 4a – 4e) demonstrate the progressive growth, deflection, and arrest of dendrites as the load and current density across the cell are varied. Growth-segments from each subfigure are highlighted in a separate color. All images for a - e were recorded using strong backlighting (i.e., light positioned below the transparent cantilever). f displays a micrograph recorded after the end of the test, recorded while the illuminating light source was positioned above the cantilever. The dotted line outlines metal growth plated without applied compression. After the load was applied, the crack-plane rotated into alignment with the out-of-the-page direction, producing the metal enclosed by the dashed line in f. All plating occurred at voltages within the LLZTO electrolyte stability window (voltage and current data available in the Supplementary Information).
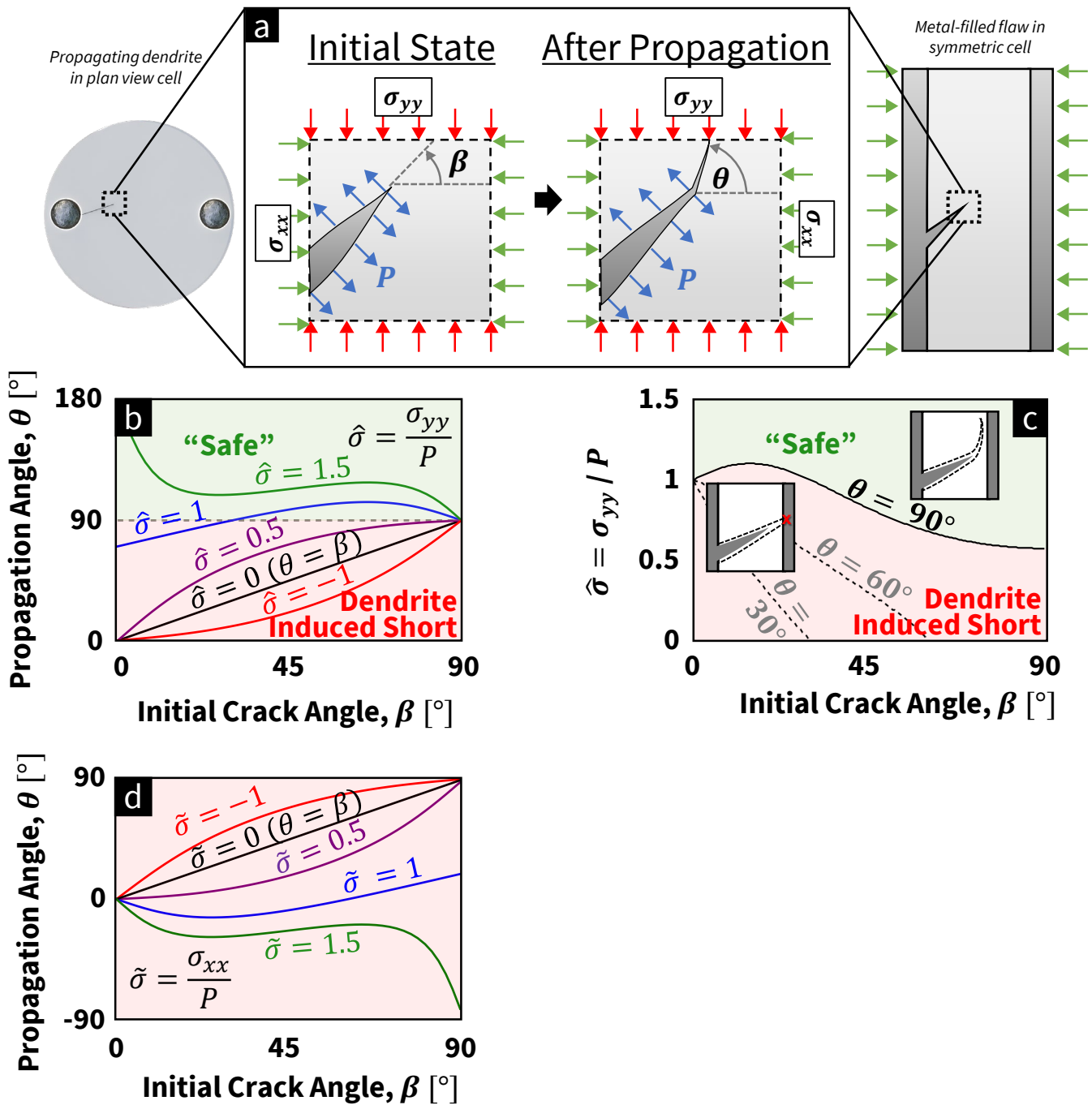
Fig. 5: Predicting Dendrite Deflection Based upon Mixed-Mode Fracture Mechanics

a) Schematic of loading conditions used in modeling kinked propagation of metal dendrites. The most energetically favorable propagation angle θ as a function of the flaw inclination β is obtained. Both angles are measured counter-clockwise from the horizontal. Two loads are present for this flaw: a plating-induced stress P acting normal to the flaw surface, with an additional load (σ_{xx} and / or σ_{yy}) due to external forces or from residual stresses present in the solid electrolyte. This model applies to two (equivalent) loading scenarios: 1) The kinking of propagating metal dendrites upon the application of applied load, shown for a plan-view cell on the left side of the subfigure, and 2) the kinking of a metal-filled flaw at the anode / electrolyte interface at the instant propagation begins (seen in the right side of the subfigure).

b) The most energetically favorable propagation angle as a function of initial crack-inclination angle β for different values of $\hat{\sigma} = \sigma_{yy}/P$. The black curve represents the case where the only stress in the system is P, (i.e., $\hat{\sigma} = 0$), such that $\theta = \beta$. Increasingly positive $\hat{\sigma}$ values represent increasing compressive loadings, which then increase the value of θ relative to that for $\hat{\sigma} = 0$, causing deflection. In the limit where $\theta = 90°$, the metal dendrite cannot reach the counter electrode regardless of the lateral dimensions of the electrolyte.

c) The value of $\hat{\sigma}$ required to produce $\theta = 90°$, $\theta = 60°$, and $\theta = 30°$ as a function of crack inclination β.

d) The most energetically favorable propagation angle θ as a function of inclination angle β for different values of $\tilde{\sigma} = \sigma_{xx}/P$. Increasingly positive $\tilde{\sigma}$ represent increasing compressive stack pressures, where stack pressures approaching the magnitude of P tend to decrease the propagation angle relative to $\tilde{\sigma} = 0$.
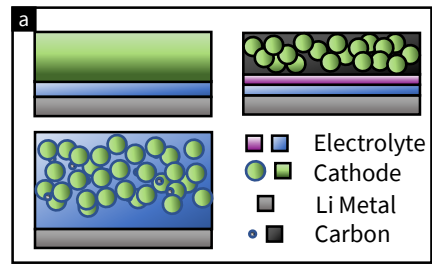
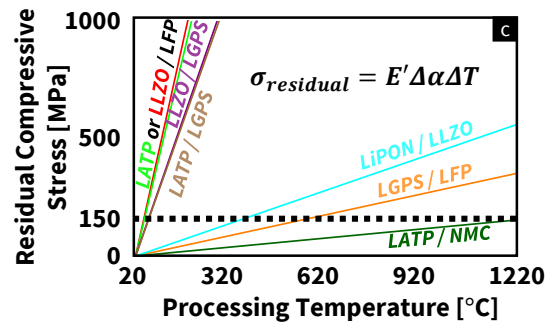| Material	α [10^{-5} K^{-1}]	α Ref. Number	E' [GPa]	E' Ref. Number
$Li_7La_3Zr_2O_{12}$ (LLZO)	1.5	23	200	40
$Li_{1+x}Al_xTi_{2-x}(PO_4)_3$ (LATP)	1.1	27	160	26,44
$Li_{10}GeP_2S_{12}$ (LGPS)	3.5	24	30	25, 43
$Li_xPO_yN_z$ (LiPON)	1	49	93	50
$LiFePO_4$ (LFP)	4.5	22	165	22
$LiNi_{0.33}Mn_{0.33}Co_{0.33}O_2$ (NMC)	1.3	45, 46	260	45

$$\sigma_{residual} = E'\Delta\alpha\Delta T$$

Fig. 6: Engineered Stresses in Conventional Cells

a) Representative geometries for sandwich-style batteries. In the upper left, a layered cathode adhered to an electrolyte-sheet and Li-anode. In the upper right, a multi-layered solid electrolyte paired with a composite-cathode and Li-metal anode. In the lower right, an example of co-sintered composite electrolyte / cathode employed against a Li-metal anode.

b) The biaxial modulus and the coefficient of thermal expansion for representative cathodes and electrolytes. Each of these materials are representative of a broader class of solid electrolytes or electrodes: LLZTO is representative of oxide electrolytes[23,40], $Li_{10}GeP_2S_{12}$ (LGPS) is representative of crystalline sulfide electrolytes,[24,25,43] $Li_{1+x}Al_xTi_{2-x}(PO_4)_3$ (LATP) is representative of LISICON electrolytes,[26,27,44] and Nickel Manganese Cobalt Oxide[45,46] (NMC) or Lithium Iron Phosphate (LFP)[22] are representative of various classes of cathodes[47,48].

c) The residual compressive stress at the solid-electrolyte/cathode interface. According to Fig. 5, compressive stresses on the order of P and larger should deflect metal dendrites, mitigating short circuiting. For representative material properties and flaw size, $P \approx 150\ MPa$. Individual series represent separate sets of electrolyte / cathode or electrolyte / electrolyte assemblies. For any given label, the first of two constituents listed (i.e., A in A / B) represents the anode-facing material. The compressive stress plotted represents the biaxial stress in the electrolyte plane, acting normally to the stack direction.